Co-opting propelling and perturbing appendages facilitates strenuous ground self-righting

Ratan Othayoth, Qihan Xuan, Chen Li*

Department of Mechanical Engineering, Johns Hopkins University

3400 N. Charles St., Baltimore, Maryland 21218, USA

*Corresponding author: chen.li@jhu.edu

Abstract

Terrestrial animals must self-right when overturned on the ground. To do so, the discoid cockroach often pushes its wings against the ground to begin a somersault but rarely succeeds in completing it. As it repeatedly attempts this, it probabilistically rolls to the side to self-right. Here, we studied whether seemingly wasteful leg flailing in this process helps. Adding mass to increase hind leg flailing kinetic energy fluctuation increased the animal's self-righting probability. We then developed a robot with similar, strenuous self-righting behavior and used it as a physical model for systematic experiments. As legs flailed more vigorously and wings opened more, self-righting became more probable. A potential energy landscape model revealed that, although wing opening did not generate sufficient kinetic energy to overcome the high pitch potential energy barrier, it reduced barriers for rolling, facilitating the small kinetic energy fluctuation from leg flailing to probabilistically overcome roll barriers to self-right.

Impact statement

When overturned terrestrial animals self-right on the ground, their seemingly wasteful yet ubiquitous flailing of appendages is crucial in providing kinetic energy fluctuation to probabilistically overcome potential energy barriers.

Introduction

Ground self-righting is a critical locomotor capability that animals must have to survive (for a review, see (Li et al., 2019)). Because a flipped-over animal is more susceptible to risks like predation, starvation, dehydration (Steyermark and Spotila, 2001), and limited mating success (Penn and Brockmann, 1995), it is crucial to be able to self-right at a high probability. Similarly, ground self-righting is critical for the continuous operation of mobile robots when performing time-sensitive tasks in the field (for a review, see (Li et al., 2017)).

Ground self-righting is an emergency response in animals. It often involves fast, desperate maneuvers (Delcomyn, 1987; Domokos and Várkonyi, 2008), increased force production compared to normal upright locomotion (Full et al., 1995), and even rapid elastic energy release (Ribak and Weihs, 2011). In particular, vigorous flailing of appendages during self-righting is a ubiquitous behavior observed across a diversity of animals, including cockroaches (Delcomyn, 1987; Sherman et al., 1977; Zill, 1986), beetles (Frantsevich and Mokrushov, 1980), mollusks (Hoffman, 1980; Weldon and Hoffman, 1979), crustaceans (Davis, 1968; Silvey, 1973), turtles (Ashe, 1970; Domokos and Várkonyi, 2008; Golubović et al., 2015; Hailey and Theophilidis, 1987), toads (Malashichev, 2016; Robins et al., 1998), rats (Bartholomew and Caswell, 1951; Winters et al., 1986), ducks (Koppányi and Kleitman, 1927), fowls (Kleitman and Koppányi, 1926), rabbits (Creery and Bland, 1980), and lambs (Vince, 1986). Such vigorous appendage motion, at first glance, appears to be a desperate, wasteful struggle.

Here, we study whether the seemingly wasteful yet ubiquitous leg flailing is beneficial to strenuous ground self-righting. Our model system is the discoid cockroach's strenuous self-righting using wings[1] (Li

[1] The discoid cockroach can also self-right using a legged strategy, by pushing its legs against the ground to rotate the body without wing use (Full et al., 1995; Li et al., 2019). Here, we focused the role of leg flailing during winged self-righting only.

et al., 2019) (Movie 1). To self-right when flipped over (Figure 1Ai), this animal often opens and pushes its wings against the ground, attempting to pitch the body over the head (the pitch mode, Figure 1Aii-iv, blue). However, the animal rarely succeeds in completing such a somersault. As the wings open, they form a triangular base of support with the animal's head (Figure 1Aii, B), and the animal often becomes trapped in this metastable state (Figure 1A, black arrows, Movie 2). The animal often makes multiple failed wing opening attempts before it probabilistically escapes from this state, and it almost always transitions to rolling to either side to self-right (the roll mode; Figure 1Aiii'-iv', red). In this process, the animal frequently and desperately flails its leg laterally as the body pitches up, even if they are held too high to touch the ground (Fig. 1B, dashed curves; Movie 2). The legs also occasionally scrape the ground, and the abdomen occasionally flexes and twists. For simplicity, we focused on the more frequent leg flailing (but see discussion).

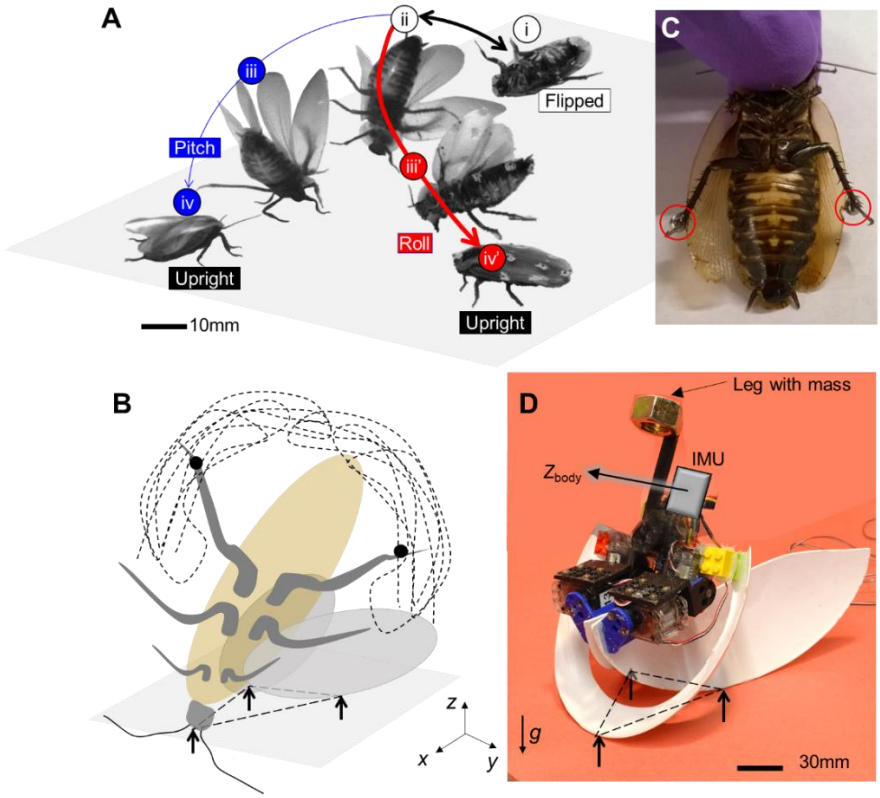

Figure 1. Leg-assisted winged self-righting. (**A**) Representative snapshots of animal during strenuous winged self-righting by pitch mode (blue) and roll mode (red). See Movie 1 for a typical trial, in which the

animal makes multiple failed attempts to pitch over the head and eventually rolls to self-right. (**B**) Schematic of metastable state with triangular support (dashed triangle), with vigorous leg flailing. Dashed curves show schematic of hind leg tip trajectory. *x*-*y*-*z* is lab frame. (**C**) Hind leg modification by attaching stainless steel spheres. (**D**) Robotic physical model in a metastable state with triangular support (dashed triangle). Black arrow shows body *Z* axis, Z_{body}. In (C) and (D), black vertical arrows show ground contact of head and two wing edges.

Recent understanding of ground self-righting using the concept of potential energy barriers provides an opportunity to elucidate the function of leg flailing. Ground self-righting is the change of body orientation during which a gravitational potential energy barrier is overcome (Domokos and Várkonyi, 2008). A previous study observing diverse self-righting strategies of cockroaches found that the animal has more body rolling in successful self-righting attempts than in failed ones (Li et al., 2019). When approximated as a rigid ellipsoid, the more an animal rolls to self-right, the lower the potential energy barrier is (Li et al., 2019). In addition, recent robotic physical modeling of winged self-righting found that inadequate wing opening results in failure to self-right by the pitch mode (Li et al., 2017), presumably because there is insufficient pitch kinetic energy to overcome the high potential energy barrier. Furthermore, it has been suggested that, when a self-righting animal is trapped in a potential energy local minimum, modest energy from appendage motion may help overcome small potential energy barriers (Domokos and Várkonyi, 2008).

Inspired by these recent insights, we hypothesized that the seemingly wasteful leg flailing provides kinetic energy fluctuation to perturb the body to probabilistically transition from being trapped in the pitch mode, which results in repeated failed attempts, to the roll mode, which results in successful self-righting. We first empirically tested the hypothesis in the animal by directly modifying the hind legs (by gluing stainless steel balls,Figure 1C) to increase leg flailing kinetic energy fluctuation and testing whether self-righting probability increased. Then, we developed a robotic physical model (Figure 1D) of leg-assisted, winged self-righting to further test the hypothesis using repeatable experiments over a wide range of

parameter space. Finally, we modeled the self-righting transition from the pitch to the roll mode as a probabilistic barrier-crossing transition on a potential energy landscape facilitated by kinetic energy fluctuation. Such an energy landscape approach was recently demonstrated to be useful in understanding locomotor transitions in complex 3-D terrain (Othayoth et al., 2020), but it was not clear whether it applies to strenuous self-righting transitions. To test this, we used the potential energy landscape to quantify the potential energy barrier that must be overcome to transition from the pitch to the roll mode, and we evaluated whether it is comparable to kinetic energy fluctuation from leg flailing. We note that, unlike the simplistic, rigid body model for calculating potential energy barriers in the previous study (Li et al., 2019), our potential energy landscape takes into account how wing opening affects potential energy and thus barriers. Our energy landscape modeling analysis is also different from that in complex 3-D terrain (Othayoth et al., 2020) because here two types of appendages work together to generate locomotor transitions. Because wing opening (primary propulsion) and leg flailing (secondary perturbation) induce different levels of kinetic energy and face different levels of potential energy barriers, their effects must be considered separately to understand the physical mechanism (see discussion of new insight this offers).

We deliberately designed and controlled our robotic physical model to achieve qualitatively similar strenuous self-righting behavior as the animal's where both wing and leg use are crucial (see discussion). The robot consisted of a head, two wings, a leg, and motors to actuate the wings and leg (Figure 1D). To simulate the animal's wing opening, both robot wings opened symmetrically by rolling and pitching about the body by the same angle (defined as wing opening amplitude, θ_{wing}; Figures 1D, 10A, Movie 3). To simplify leg flailing of the animal, the robot used a simple pendulum-like leg which oscillated in the coronal plane by the same angle to either sides (defined as leg oscillation amplitude, θ_{leg}; Figures 1D, 10A, Movie 3). We repeatedly opened and closed the robot's wings while oscillating it legs to generate repeated attempts observed in the animal. A previous study found that sufficiently large or asymmetric wing opening alone guarantees successful self-righting (Li et al., 2017, 2016). Here, to study the effect of leg flailing kinetic energy fluctuation under the most strenuous condition, we chose to open both wings symmetrically and

only used sufficiently small θ_{wing} with which the robot did not always self-right with wing opening alone. We emphasize that our goal was not to simply achieve successful self-righting in a robot.

We chose to focus our energy landscape modeling on the robotic physical model (Aguilar et al., 2016) because it offers two major advantages. First, the animal's complex 3-D motion with many degrees of freedom is difficult to quantify. It would take ~540 hours to track our animal dataset (~5 seconds each trial at 200 frames/s, with 3 markers on the body, each wing, and each leg) to quantify 3-D motion required for calculating the energy landscape, and wing motion is often impossible to quantify due to occlusion under the body. By contrast, the robot's simpler mechanical design, motor actuation, and an onboard IMU sensor allowed easier reconstruction of its 3-D motion. Second, the animal's wing opening and leg flailing are highly variable (Xuan and Li, 2020), and cannot be controlled. This results in the potential energy landscape varying substantially from trial to trial and makes it difficult to evaluate how the system behaved probabilistically on the landscape. By contrast, the robot's controlled variation of wing opening and leg flailing allowed us to do so. This enabled us to accurately measure kinetic energy fluctuation, calculate the potential energy landscape, and reconstruct how the system state behaved on the landscape.

Results

Leg flailing facilitates animal self-righting

As leg modification increased the animal's kinetic energy fluctuation during leg flailing (Figure 2A), the animal's probability to self-right using wings increased (Figure 2B, Movie 4; $P < 0.0001$, $F_{1, 29} = 93.38$, mixed-design ANOVA). These animal observations supported our hypothesis. We verified that leg modification did not change the animal's behavioral preferences of using the winged and legged self-righting strategies (Figure 9).

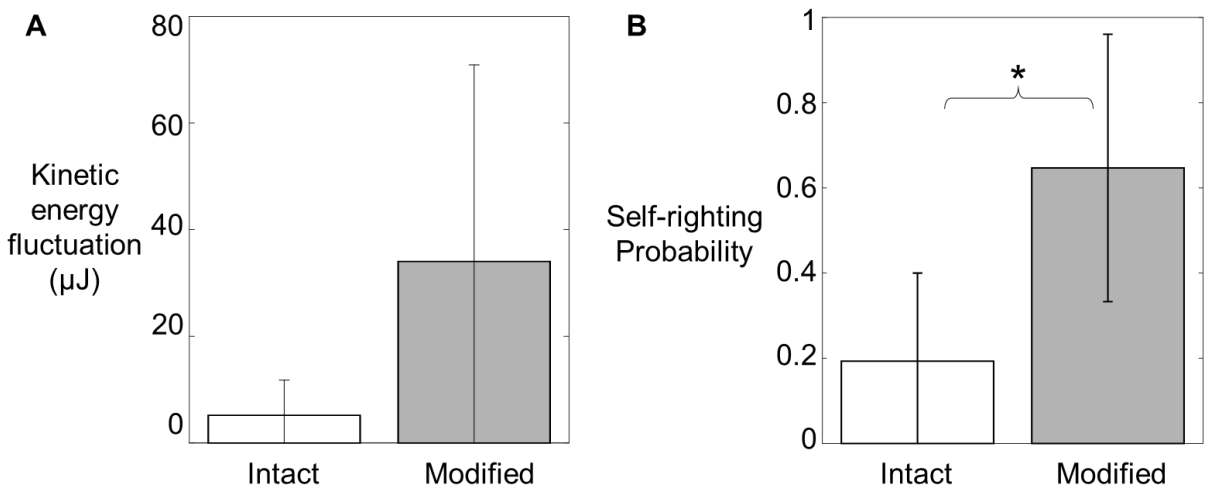

Figure 2. Animal's self-righting probability increases with leg flailing kinetic energy fluctuation. Comparison of kinetic energy fluctuation (**A**) and self-righting probability (**B**) between animals with intact and modified legs. Error bars show ± s.d. Asterisk indicates a significant difference ($P < 0.0001$, $F_{1, 29} = 93.38$, mixed-design ANOVA for probability, $N = 30$ animals, $n = 150$ trials each with intact and modified legs). Source: Figure_2B_Source_Data.xlsx.

Leg flailing facilitates robot self-righting

The robot's self-righting performance increased with its leg flailing kinetic energy fluctuation over a wide range of wing opening amplitudes θ_{wing} (Figure 3). For each θ_{wing} tested, as leg flailing kinetic energy fluctuation increased with leg oscillation amplitude θ_{leg} (Figure 3A, $P < 0.0001$, repeated-measures ANOVA), self-righting probability increased (Figure 3B, $P < 0.005$, chi-squared test) and reached one at higher θ_{leg}. Meanwhile, the number of attempts required for self-righting decreased (Figure 3C, Movie 5; $P < 0.05$, repeated-measures ANOVA). At the maximal θ_{leg} tested (45°), the robot always self-righted (Figure 3B) and always did so in the first wing opening attempt (Figure 3C). Together, these robot results further verified our hypothesis over a wide range of parameter space.

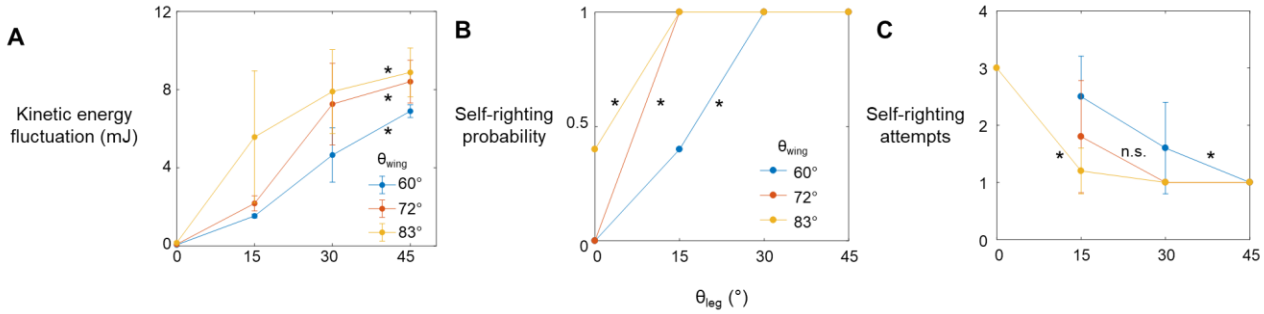

Figure 3. Robot self-righting performance increases with roll kinetic energy fluctuation. Kinetic energy fluctuation (**A**), self-righting probability (**B**), and number of attempts to self-right (**C**) of robot at different wing opening amplitudes θ_{wing}, as a function of leg oscillation amplitude θ_{leg}. Error bars are ± s.d. Asterisks indicate a significant dependence on θ_{leg} at each θ_{wing} (kinetic energy fluctuation: $F_{1, 18}$ = 239.97, 112.98, and 38.08 for θ_{wing} = 60°, 72°, and 83°, respectively, repeated-measures ANOVA, n = 20 trials at each θ_{wing}; probability: $\chi^2(1, n = 20)$ = 20.19, $P < 0.0001$, for θ_{wing} = 60°, $\chi^2(1, n = 20)$ = 22.49, $P < 0.0001$, for θ_{wing} = 72°, and $\chi^2(1, n = 20)$ = 10.18, P = 0.0014, for θ_{wing} = 83°, nominal logistic regression; number of attempts: $F_{1, 10}$ = 8.62, P = 0.015 for θ_{wing} = 60°, $F_{1, 13}$ = 3.90, P = 0.069 for θ_{wing} = 72°, and $F_{1, 15}$ = 13.66, P = 0.002 for θ_{wing} = 83°, ANOVA. n.s. indicates no statistical significance ($P > 0.05$). Source: Figure_3_Source_Data.xlsx.

Robot self-righting resembles animal's

The robot's winged self-righting resembled that of the discoid cockroach (Figure 4A, Movie 5). Because we chose to use sufficiently small wing opening amplitudes, it often took the robot multiple wing opening attempts to self-right probabilistically, similar to the animal. As the wings opened, the body pitched up (Figure 4Ai)). In failed attempts, after the wings were fully open, the body was unable to continue to pitch over the head (Figure 4Aiii-iv, blue). Instead, it was trapped in the metastable state with triangular support (Figure 4Aii)) before becoming upside-down again as the wings closed (Figure 4Ai). In successful attempts, the robot was able to escape the metastable state probabilistically and always self-righted by rolling to either side (Figure 4Aiii'-iv', red). The robot never lifted off the ground during self-righting. All these observations were similar to animal observations. This meant that the robot can serve as a good

physical model to understand the mechanism of the role of leg flailing during strenuous winged self-righting.

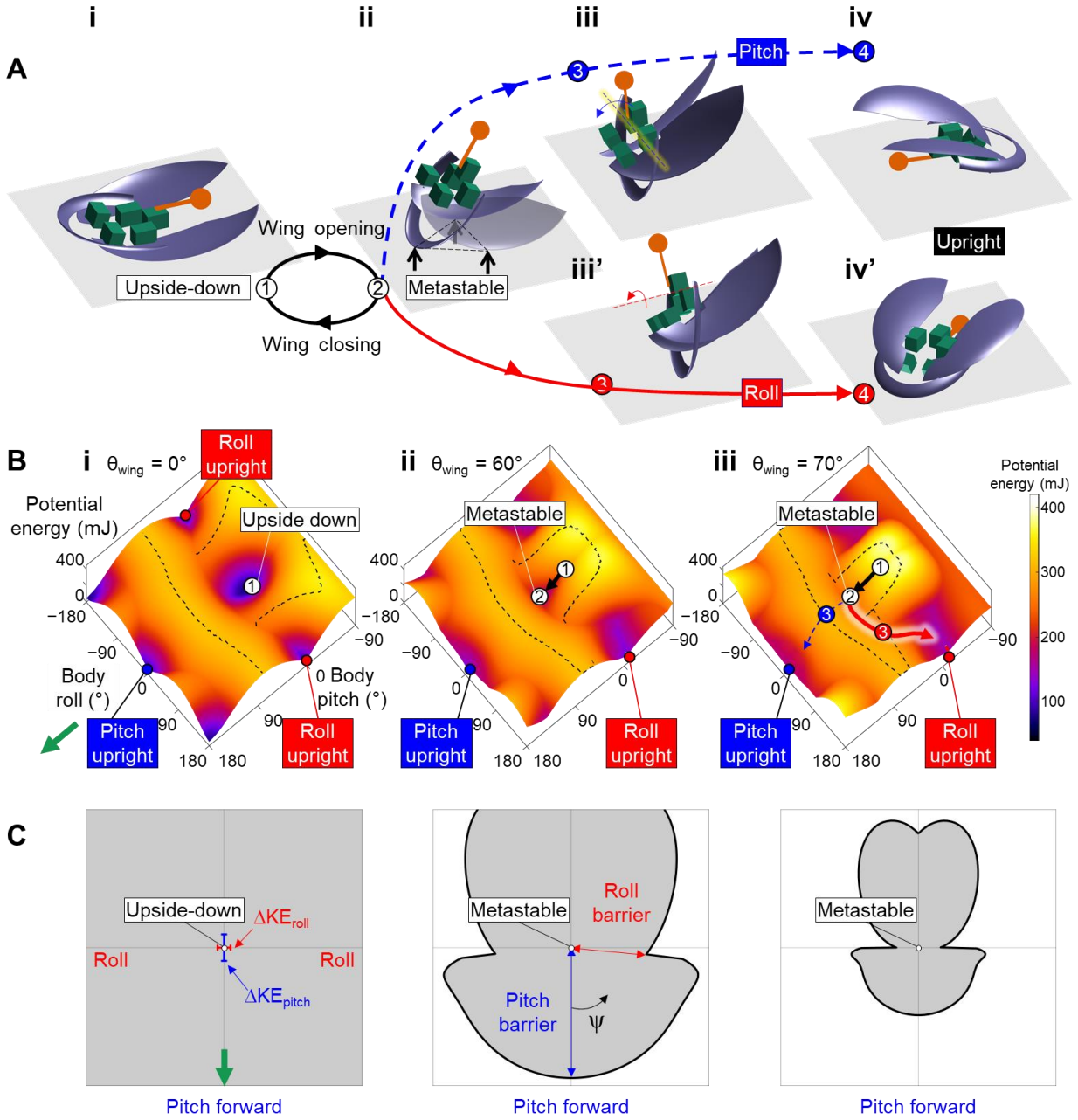

Figure 4. Robot's self-righting motion and potential energy landscape modeling. (**A**) Snapshots of reconstructed robot upside down (i), in metastable state (ii), self-righting by pitch (iii) and roll (iii') modes, and upright afterwards (iv, iv'). (**B**) Snapshots of potential energy landscape at different stages of wing

opening angles in (A) i, ii, iii. Dashed black curves are boundary of upside-down/metastable basin. Black, dashed blue, and red curves are representative trajectories of being trapped in metastable basin, self-righting by pitch mode, and self-righting by roll mode, respectively. (**C**) Polar plot of potential energy barrier to escape upside down or metastable local minimum along all directions in pitch-roll space. Green arrow in (i) shows direction of upright minima at pitch = 180° (i.e., $\psi = 0°$). Blue and red error bars in (i) show pitch kinetic energy and roll kinetic energy fluctuation. Blue and red arrows in (ii) define pitch and roll barriers. Source: Figure_4_Source_Data Bi-iii, Ci-iii.

Potential energy landscape changes as wings open

The robot's potential energy landscape over body pitch-roll space changed as the wings opened (Figure 4, Movie 6). When the wings are fully closed, the potential energy landscape had a local minimum at near zero body pitch and roll (Figure 4Bi, white dot, Movie 6, top right). This is intuitive because either body pitching or rolling from upside down increased center of mass height and thus gravitational potential energy. Hereafter, we refer to this local minimum basin as the upside-down basin. The landscape also had three other local minima corresponding to the body being upright. The local minimum at body pitch = 180° and roll = 0° (Figure 4B, blue dots) can be reached by pitching forward (pitch mode; Figure 4Aiii-iv, 4Biii, Movie 6, blue curve), and the two local minima at body pitch = 0° and roll = ±180° (Figure 4B, red dots) can be reached by rolling left or right (roll mode; Figure 4Aiii'-iv', 4Biii, Movie 6, red curve). Hereafter, we refer to these upright local minimum basins as pitch upright and roll upright basins, respectively. There was a fourth upright basin[2] at body pitch ~ −170° and roll = 0°, which corresponds to self-righting by pitching downward. However, such a motion was not observed in the animal or robot, so we did not consider this upright basin.

[2] The body pitch location of the fourth local minimum varies within [−180°, −162°] as the wing opening angle changed from 0° to 90°.

As the wings opened, the potential energy landscape changed. The upside-down basin evolved into a metastable basin around a local minimum with a positive pitch and zero roll (Figure 4Bii, white dot). This local minimum corresponded with the metastable state with triangular support (Figure 4Aii). The more the wings opened, the higher the pitch of this local minimum was. To self-right via either the pitch mode (Figure 4Aiii-iv) or the roll mode (Figure 4Aiii'-iv'), the system state must escape from the metastable basin to reach either the pitch upright basin (Figure 4Biii, dashed blue curve) or one of the roll upright basins (e.g., Figure 4Biii, red curve).

Self-righting transitions are barrier-crossing transitions on potential landscape

Reconstruction of the robot's 3-D motion revealed that self-righting transitions are probabilistic barrier-crossing transitions on the potential energy landscape (Figure 5, Movies 6-8). The system state was always attracted to a landscape basin. At the beginning of a self-righting attempt, the system state was in the upside-down basin. As the wings opened, the system state was attracted towards the metastable basin, which shifted towards the positive pitch direction. In failed attempts, as the wings opened and closed, the system state was trapped in and moved along with the metastable basin back and forth (Figure 5, black curves). By contrast, in successful attempts, the system state probabilistically escaped by crossing a potential energy barrier (Figure 4B, dashed black curves) to find a roll upright basin (Figure 5, white curves, Movies 7, 8).

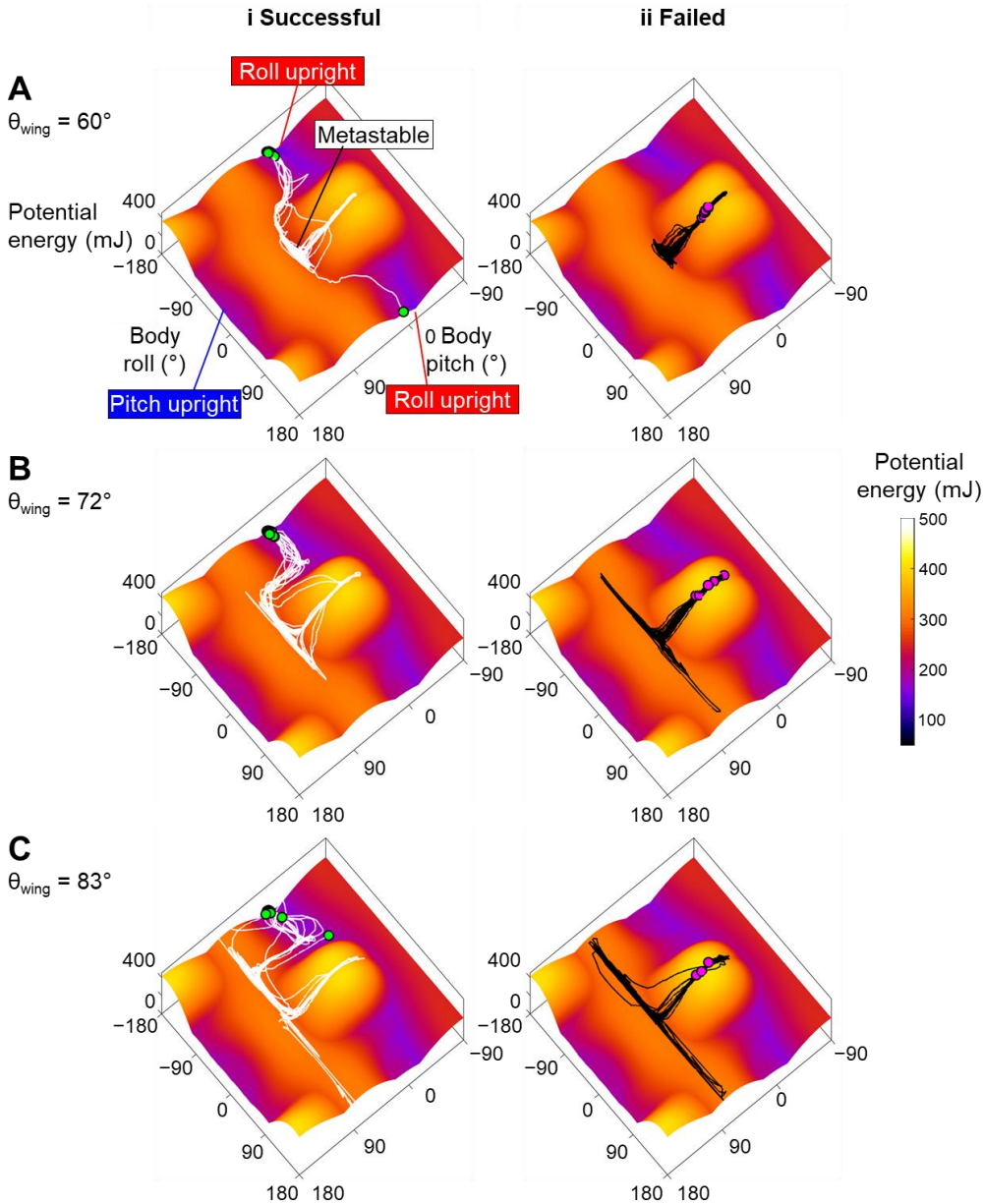

Figure 5. Robot state trajectories on potential energy landscape. (**A**) θ_{wing} = 60°. (**B**) θ_{wing} = 72°. (**C**) θ_{wing} = 83°. Columns i and ii show trajectories for successful (white) and failed (black) self-righting attempts, respectively. Green and pink dots show the system state for successful and failed attempts, respectively. At higher θ_{wing}, the high body roll of state trajectories in failed attempts is an artifact from the singularity in Euler angle convention at near 90° body pitch. n = 20 trials for each θ_{wing}. Source: Figure_5_Source_Data_Ai, iii; Bi, ii; Ci, ii.

Roll barrier is lower than pitch barrier

The energy landscape model allowed us to quantify the potential energy barrier to be overcome to self-right via the pitch and roll modes. The potential energy barrier to transition from the metastable to an upright basin depended on the direction along which the system moved in the body pitch-roll space (Figure 4C; Supplementary Video 5, bottom right). We defined the pitch and roll barriers as the minimal barriers to escape from the metastable local minimum towards the pitch and roll (Figure 4C, blue and red arrow) upright basins. For any given wing opening angle, the roll barrier was always lower than the pitch barrier.

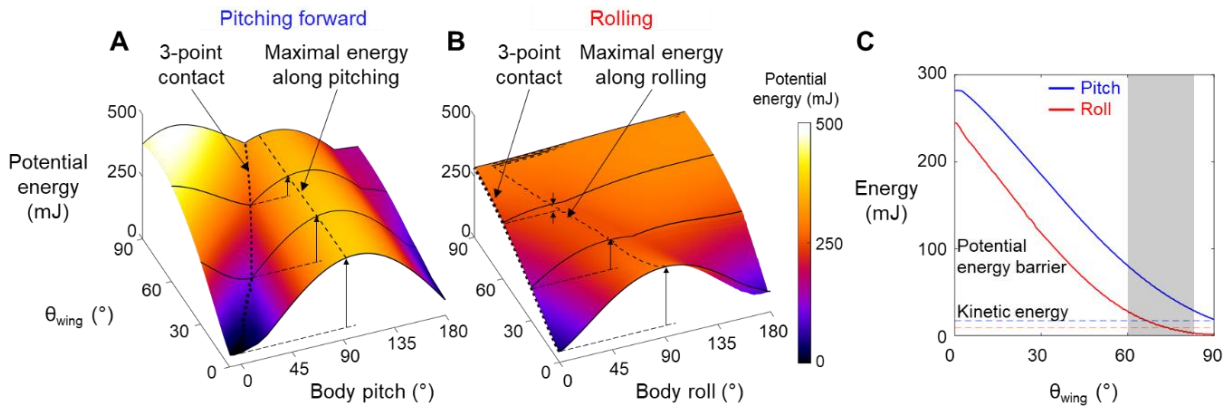

Figure 6. Robot transition barriers for self-righting by pitching or rolling. (**A**) Potential energy of robot self-righting by pitching as a function body pitch and wing opening amplitude θ_{wing}. (**B**) Potential energy of robot self-righting by rolling as a function body roll and θ_{wing}. Dotted black curves in A and B show energy of metastable local minimum. Dashed black curve shows maximal energy when pitching forward or rolling from metastable state. Vertical arrows define pitch (A) and roll (B) barrier at a few representative θ_{wing}. (**C**) Pitch (blue) and roll (red) barrier as a function of θ_{wing}. Blue and red dashed lines show pitch kinetic energy and roll kinetic energy fluctuation, respectively. Gray band shows range of θ_{wing} tested. Source: Figure_6_Source_Data_A, B, C.

Barrier reduction by wing opening facilitates self-righting via rolling

Our model calculations also showed that, as θ_{wing} increased, both the pitch and roll barrier decreased monotonically (Figure 6C, Movie 7, bottom left). As the wings open to the range of θ_{wing} tested (Figure 6C, gray band), the pitch barrier (Figure 6C, solid blue curve) was still much greater than the average pitch kinetic energy (dashed blue line). By contrast, the roll barrier (solid red curve) was lowered to similar levels of the average roll kinetic energy fluctuation (dashed red line). These findings suggested that, although wing opening did not generate sufficient kinetic energy to self-right by pitching, it facilitates the small roll kinetic energy fluctuation to induce self-righting by rolling.

Wing opening kinetic energy is insufficient for self-righting by pitching

To test whether this was indeed the case, we used the reconstructed 3-D motion and potential energy landscape model to analyze the robot's mechanical energy budget, defined as kinetic energy minus potential energy barrier, for all the observed self-righting attempts in both the pitch and roll directions.

For all attempts, as the wings opened, pitch kinetic energy initially increased as the robot accelerated and began pitching up, peaked in the middle of wing opening, and then diminished as the wings became fully open (Figure 7A). Meanwhile, the pitch barrier decreased and remained minimal as the wings were fully open (Figure 7B). Because pitch kinetic energy remained smaller than the pitch barrier, there was always a deficit in pitch mechanical energy budget (Figure 7C, D), even at the maximal θ_{wing} and θ_{leg} tested (Figure 7E). This deficit precluded the robot from pitching forward to self-right and explained the absence of the pitch mode in experiments. Even for successful attempts via the roll mode, the pitch mechanical energy budget remained negative (Figure 7Di). These results confirmed that pitch kinetic energy from wing opening was indeed insufficient for overcoming the pitch barrier to self-right by pitching.

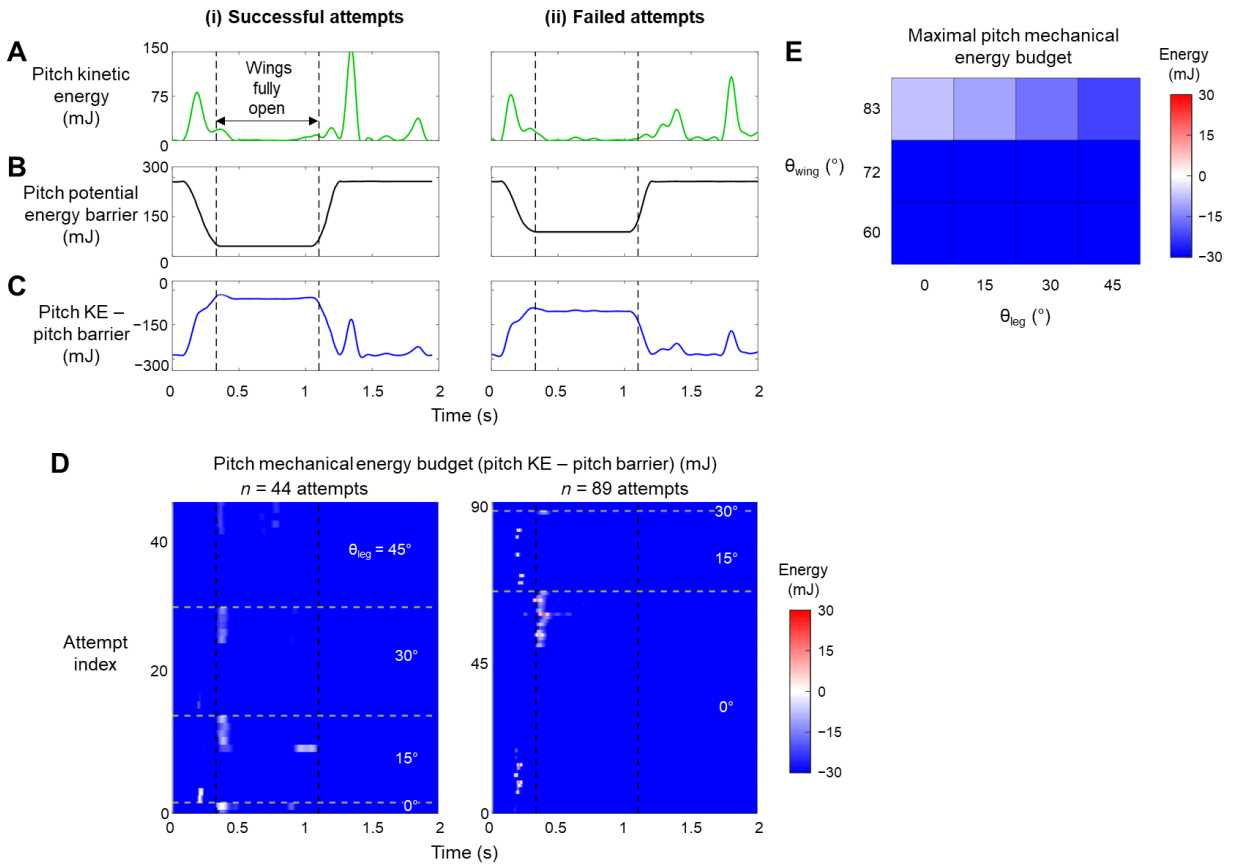

Figure 7. Robot pitching energy budget. (**A**) Pitch kinetic energy, (**B**) pitch barrier, and (**C**) mechanical energy budget in pitch direction, all as a function of time, over one wing opening attempt in a representative trial. Between two vertical dashed lines is when wings are held fully open. (**D**) Mechanical energy budget in pitch direction as a function of time over all wing opening attempts from all trials. The attempts are grouped along y axis into different θ_{leg}. For each group of different θ_{leg}, the attempts are further grouped by different θ_{wing}. Columns (i) and (ii) are successful and failed attempts. (**E**) Maximal pitch mechanical energy budget when wings are fully open as a function of θ_{wing} and θ_{leg}. Red and blue show positive and negative energy budget, respectively. *n* = 134 attempts. Source: Figure_7_Source_Data.

Leg flailing kinetic energy fluctuation is sufficient for self-righting by rolling

For all attempts, as the wings fully opened, the roll barrier decreased and diminished to a minimum (Figure 8B). Meanwhile, leg flailing resulted in small roll kinetic energy fluctuation that was sometimes

comparable to the minimal roll barrier (Figure 8A). This resulted in occasional surpluses in roll mechanical energy budget (Figure 8C, D). In addition, the maximal roll mechanical energy budget and its surplus increased with both θ_{wing} and θ_{leg} (Figure 8E, $P < 0.0001$ for each θ_{wing} and each θ_{leg}, ANOVA, $n = 134$ attempts). These results meant that sufficiently large wing opening drastically reduced the roll barrier and facilitated the small roll kinetic energy fluctuation to perturb the system to probabilistically overcome the roll barrier and self-right by rolling.

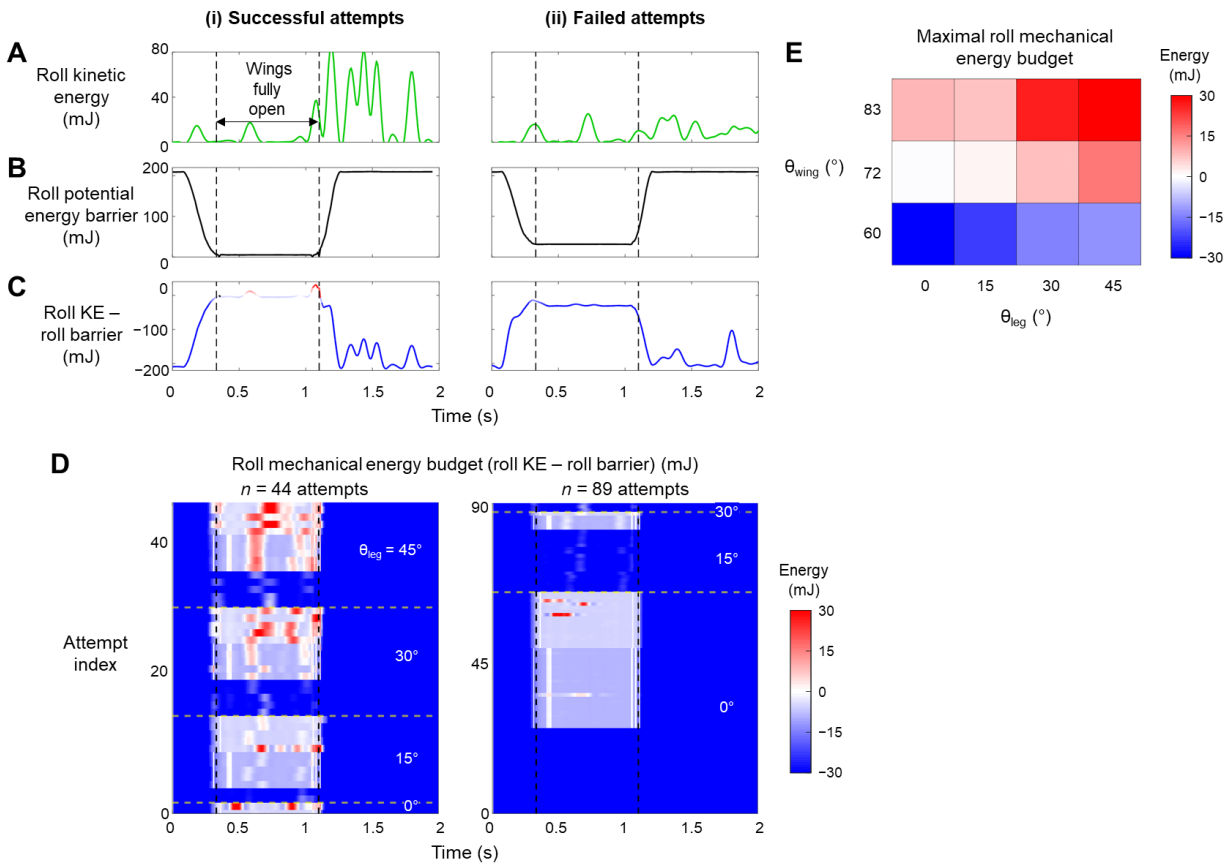

Figure 8. Robot rolling energy budget. (**A**) Roll kinetic energy, (**B**) roll transition barrier, and (**C**) mechanical energy budget for escaping metastable basin by rolling sideways, as a function of time over one wing opening attempt. Between two vertical dashed lines is when wings are held fully open. (**D**) Mechanical energy budget to self-right by rolling as a function of time over each wing opening attempt across all trials. The attempts are grouped along y axis into different θ_{leg}. For each group of different θ_{leg}, the attempts are further grouped by different θ_{wing}. Columns (i) and (ii) show results for successful and failed attempts. (**E**)

Maximal roll mechanical energy budget when wings are fully open as a function of θ_{wing} and θ_{leg}. Red and blue show positive and negative energy budget, respectively. ($F_{1, 56}$ = 332.46 for θ_{wing} = 60°, $F_{1, 32}$ = 11.71 for θ_{wing} = 72°, and $F_{1, 40}$ = 265.34 for θ_{wing} = 83°, $P < 0.0001$ for each θ_{wing}, ANOVA; $F_{1, 64}$ = 155.93 for θ_{leg} = 0°, $F_{1, 33}$ = 161.43 for θ_{leg} = 15°, $F_{1, 16}$ = 442.35 for θ_{leg} = 30°, and $F_{1, 13}$ = 107.62 for θ_{leg} = 45°, $P <$ 0.0001 for each θ_{leg}; ANOVA, n = 134 attempts). Source: Figure_8_Source_Data.

Discussion

In this study, we integrated animal experiments, robotic physical modeling, and energy landscape modeling to reveal the physical principles and elucidate the physical mechanisms of strenuous, leg-assisted, winged ground self-righting. We discovered that kinetic energy fluctuation from leg flailing helps probabilistically cross barriers on a potential energy landscape to self-right, analogous to noise-activated escape of a microscopic particle in a potential energy well (Hanggi, 1986; Kramers, 1940). Although neither wing opening nor leg flailing alone is sufficient for self-righting, wing opening diminishes the potential energy barrier in the roll direction and facilitates the small roll kinetic energy fluctuation from leg flailing to overcome it.

The animal's strenuous winged self-righting behavior is more complex and variable than the robot's, with multiple legs flailing, occasional leg scraping the ground, and occasional abdomen flexion and twisting. Despite this, the results from our robotic physical model, designed and controlled to generate qualitatively similar behavior, suggested that the most fundamental mechanics can be explained by probabilistic barrier crossing transitions activated by kinetic energy fluctuation. This is because the perturbing effect of these additional complexities can also be modeled as kinetic energy fluctuation. They may slightly shift the center of mass and thus change the potential energy landscape at a fine-grain level (see below). However, the topology of the landscape—having a persistent metastable basin in the triangular base of support—should be preserved in strenuous winged self-righting. Otherwise, the animal should simply self-right without needing kinetic energy fluctuation.

Expanding energy landscape-dominated regime of locomotion

It was recently suggested that there is an "energy landscape-dominated" regime of locomotion (Othayoth et al., 2020)—when there are large potential energy barriers comparable to or exceeding kinetic energy and/or mechanical work generated by each propulsive cycle or motion, an energy landscape approach is useful for understanding probabilistic locomotor transitions. Our findings supported this notion and expanded the range of this regime of from locomotor transitions in complex 3-D terrain to strenuous self-righting transitions. More broadly, this commonality supports the idea that there may be general principles of locomotor transitions across different forms, and an energy landscape approach may be useful for testing and comparing across systems (different species, environment, modes, etc.) (Othayoth et al., 2020).

By separating the analysis of primary propulsion (wing opening) and secondary perturbation (leg flailing), our energy landscape modeling also offers new insight that animals and robots can modify the potential energy landscape (here by opening wings) to lower the barrier to facilitate the use of kinetic energy (here from leg flailing) to probabilistically make locomotor transitions. This complements the naïve, "vibrate like a particle" strategy discovered from the previous study (Othayoth et al., 2020).

We note that our potential energy landscape does not model system dynamics and only considers conservative gravitational force. Adding stochastic, non-conservative forces to model how the system "diffuses" across landscape barriers (Bryngelson and Wolynes, 1989) may lead to statistical physics models that describe probabilistic barrier-crossing dynamics of strenuous self-righting activated by kinetic energy fluctuation.

Leg flailing is not wasteful but crucial for strenuous self-righting

Our results provided evidence that the seemingly wasteful appendage flailing in the discoid cockroach (and likely other species) is a crucial component of the self-righting behavior. Ground self-righting is a strenuous locomotor task (Brackenbury, 1990; Camhi, 1977; Domokos and Várkonyi, 2008;

Full et al., 1995; Li et al., 2019). For the discoid cockroach, self-righting requires overcoming potential energy barriers an order of magnitude greater (Li et al., 2019) than the mechanical energy requirement of steady-state, medium speed running (Full and Tu, 1990) or exerting ground reaction forces eight times greater than that during running (Full et al., 1995). Because it costs so much energy, whether each self-righting attempt succeeds or fails can make the difference between life and death. Our study showed that, when the primary appendages for self-righting cannot generate sufficient kinetic energy to self-right by crossing high potential energy barriers, flailing of secondary appendages becomes crucial for inducing probabilistic transitions to cross lower barriers, thereby increasing the chance of self-righting. Importantly, although together they make self-righting more probable.

Leg flailing as an exaptation

Similar to cockroach wings that can fold against the body into a streamlined "shell" to aid obstacle traversal (Li et al., 2015) and opened to push against the ground for self-righting propulsion (Li et al., 2019), our study demonstrated that leg flailing is a yet another of the discoid cockroach's biological exaptation (Gould and Vrba, 1982). Here, legs that evolved primarily for propelling locomotion is co-opted to generate perturbation during strenuous ground self-righting. Although our robotic physical model only used a simple pendulum "leg" to demonstrate these principles and mechanisms, field-ready terrestrial robots should co-opt existing appendages initially dedicated to propulsion for secondary functions such as self-righting to achieve multi-functionality (Johnson et al., 2012; Springthorpe, 2016).

Energy landscape for understanding self-righting behaviors

Our work demonstrated that potential energy landscape modeling is a useful for understanding self-righting behaviors. During self-righting, which is often strenuous, an animal or robot is often not capable of injecting sufficient mechanical energy to overcome large potential energy barriers. Thus, they are often attracted to and trapped in metastable basins on the potential energy landscape. Although the potential energy landscape over configuration space does not yet capture system dynamics, analyzing how the

locomotor's morphology and self-deformation (and the environment) together define landscape basins allows understanding of how they constrain self-righting behavior. For example, in our model system, the stereotyped body motion—pitching up and down repeatedly, then rolling to the side—directly results from how the metastable basin evolves and changes height (and thus changing the roll barrier relative to kinetic energy fluctuation) as the configuration changes. This provided direct evidence that the stereotypy of animal behavior (Berman, 2018) emerges from interaction of their neuromechanical systems with the physical environment (Dickinson et al., 2000).

Although we only demonstrated it in a model system, the energy landscape approach can in principle be applied to more complex and different self-righting behaviors. For example, for leg-assisted, winged self-righting, we can add degrees of freedom for multiple legs flailing, abdomen flexion and twisting, and even passive wing deformation (due to load) (Li et al., 2019) to create fine-grained energy landscapes to understand how the hierarchy (Berman, 2018) of body and appendage behaviors during self-righting is constrained by locomotor-ground interaction. We can also understand legged self-righting by modeling how the legs and deformable abdomen (Li et al., 2019) affect the potential energy landscape. This broad applicability will be particularly useful for comparative studies across species, such as understanding why some cockroach species' self-righting is more dynamic than others (Li et al., 2019). Similarly, an energy landscape approach will also inform the design and control of self-righting robots (e.g., (Caporale et al., 2019; Kessens et al., 2012)). However, this approach does not apply to highly dynamic self-righting strategies, such as self-righting using jumping (Bolmin et al., 2017; Kovac et al., 2008), where kinetic energy far exceeds the potential energy barrier.

Potential importance of wing-leg coordination

Our result that wing opening reduces the roll barrier for leg flailing to overcome suggests that wing-leg coordination may be important for strenuous self-righting of the discoid cockroach. However, treating leg flailing as an average kinetic energy fluctuation does not allow understanding of this interesting question. We have created a simplified template model to study how wing-leg coordination affects

mechanical energy accumulation during self-righting (Xuan and Li, in revision 2) and developed a robot simulation to understand the role of the unusually large randomness observed in the animal's wing-leg coordination (Xuan and Li, in revision 1).

Materials and methods

Animals

For animal experiments, we used 30 adult male *Blaberus discoidalis* cockroaches (Figure 1B) (Pinellas County Reptiles, St Petersburg, FL, USA), as females were often gravid and under different load-bearing conditions. Prior to experiments, we kept the animals in individual plastic containers at room temperature (24 ºC) on a 12h:12h light: dark cycle and provided water and food (rabbit pellets) *ad libitum*. Animals weighed 2.6 ± 0.2 g and measured 5.3 ± 0.2 cm in length, 2.3 ± 0.1 cm in width, and 0.8 ± 0.1 cm in thickness. All data are reported as mean ± s.d. unless otherwise specified.

Animal leg modification

To study the effect of leg flailing, we directly modified both hind legs of the animal. We attached stainless steel spheres of diameter 0.32 cm and mass 0.14 g (McMaster-Carr, Elmhurst, IL, USA) to the tibia-tarsus joint of both hind legs (Figure 1A, Movie 4, right) using ultraviolet curing glue (BONDIC, Ontario, Canada). We verified that the added mass increased the kinetic energy during leg flailing (Figures 2A, 11; see section 'Animal kinetic energy fluctuation').

Animal self-righting behavior

We verified that the animal's self-righting behavior did not change with leg modification. The discoid cockroach can use two strategies to self-right (Li et al., 2019)—either by repeatedly opening and closing its wings while flailing the legs (winged self-righting), or by pushing its legs against the ground

without opening the wings (legged self-righting). To compare the animal's self-righting behavior before and after leg modification, for each trial, we visually examined the videos and identified sections of winged and legged self-righting. We measured the percentage of time that the animal spent on winged and legged self-righting within each trial. Then, for each treatment, we pooled all trials of all animals to calculate the average percentage of time spent on legged and winged attempts (Figure 9). We found that the time that the animal spent on each strategy did not change with leg modification ($P > 0.05$, mixed-design ANOVA), suggesting that its behavior did not change.

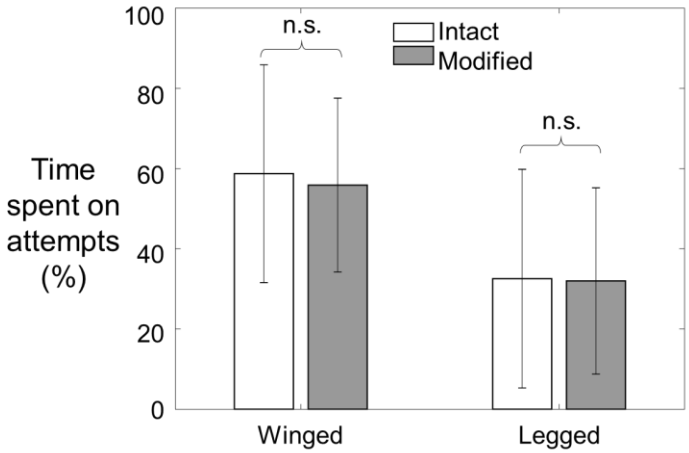

Figure 9. Leg modification did not change animal self-righting behavior. Comparison of percentage of time spent on winged and legged self-righting between animals with intact (white) and modified (gray) legs. Error bars are ± s.d. n.s. indicates no significant difference ($P = 0.19$ and $F_{1,269} = 1.71$ for winged, $P = 0.78$ and $F_{1,269} = 0.07$ for legged, mixed-design ANOVA). $N = 30$ animals, $n = 150$ trials for each treatment. Source: Figure_9_Source_Data.

Robotic physical model

The robot consisted of a head, two wings, a leg, and four motors to actuate the wings and one to actuate the leg (Table 1, Figures 1D, 10A, Movie 3). The head and wings were cut from two halves of a thin ellipsoidal shell thermo-formed (Formech 508FS, Middleton, WI, USA) from 0.16 cm thick polystyrene plastic sheet (McMaster-Carr, Elmhurst, IL, USA). We connected different parts using joints

3-D printed using PLA (Ultimaker 2+, Geldermalsen, Netherlands) (Figure 1D). We used DC servo motors (Dynamixel XL-320, ROBOTIS, Lake Forest, CA, USA) to actuate both the wings and the leg.

To measure the robot's 3-D orientation (roll, pitch, and yaw angles), we attached an inertial measurement unit (IMU) (BNO055, Adafruit, New York, NY, USA) near its center of mass. We used the Robot Operating System (Quigley et al., 2009) to send actuation signals for the wing and leg motors and record IMU data. To ensure a constant voltage for repeatable experiments, we used an external 8 V voltage source (TP3005DM, TEK Power, Montclair, CA, USA) to power the robot. We ensured that the wires connected to the robot (for powering robot and sending/acquiring signals) were loose and did not interfere with robot motion.

Table 1. Mass distribution of the robot.

Component	Mass (g)
Head	13.4
Leg rod	4.3
Leg added mass	51.5
Leg motor	28.6
Two wings	57.4
Two wing pitch motors	56.0
Two wing roll motors	48.8
Total	260

Animal experiment protocol

For animal experiments, we used a flat, wooden surface (60 cm × 60 cm) covered with cardstock and walled with transparent acrylic sheets as the righting arena. Four 500 W work lights (Coleman Cable, Waukegan, IL, USA) illuminated the arena for high speed imaging. We maintained the arena at a temperature of 40 ± 2 ºC during experiment. We used two synchronized cameras (Fastec IL5, Fastec Imaging, San Diego, CA, USA) at 200 frames s^{-1} and 200 μs shutter time to record the self-righting

maneuver from top (1200 × 1080 pixels) and side (1200 × 400 pixels) views, with a small lens aperture to maximize the focal depth of field.

For each trial, we first started video recording and then held the animal upside-down by its pronotum and gently released it from a height of ~1 cm above the center of the righting arena. If the animal self-righted or 10 seconds elapsed after it began its self-righting attempt, it was picked up and video recording was stopped. After each trial, we returned the animal to its container and allowed it to rest for ~30 minutes before its next trial to minimize the effects of fatigue (Camhi, 1977).

We tested 30 animals, each with five trials with its hind legs intact and then modified, resulting in a total of 300 accepted trials (N = 30 animals, n = 150 trials for each leg treatment). We excluded trials in which the animal collided with the walls of the righting arena or moved out of both the camera views during self-righting attempts.

Robot experiment protocol

For robot experiments, we used a level, flat, rigid wooden surface (60 cm × 60 cm) covered with sandpaper as the righting arena. We used two synchronized webcams (Logitech C920, Logitech, Newark, CA, USA) at 30 frames s^{-1} and a resolution of 960 × 720 pixels to record the experiment from top and side views (Movie 5). Using the onboard IMU, we recorded the robot body orientation relative to the lab coordinate system (X-Y-Z in Figure 1D) at ~56 Hz and synchronized them with motor actuation angles (Figure 10C, Movie 5, bottom right).

At the beginning of each trial, we placed the robot upside-down (Figure 4Ai) on the arena, with its wings closed and leg aligned with the body midline, and started video recording. We then actuated the robot to repeatedly open and close its wings at a frequency of 2 Hz and oscillate its legs at 2.5 Hz to self-right. Because the animal was more likely to move its leg before wings at the start of self-righting (59% of intact leg trials and 81% of modified leg trials), for non-zero leg oscillation amplitudes, the first wing opening was started after completing one cycle of leg oscillation (0.4 s). We then controlled the positions of motors to achieve the commanded wing opening θ_{wing} and leg oscillation amplitude θ_{leg} (Figure 10B, solid blue and

red curves show commanded trajectories of θ_{wing} and θ_{leg}, respectively; Movie 5). If the robot did not self-right after five wing opening attempts (10 s), we powered down the robot, stopped video recording, and reset the robot for the next trial.

We tested self-righting performance of the robot by systematically varying leg oscillation amplitude θ_{leg} (0°, 15°, 30°, 45°) and wing opening amplitude θ_{wing} (60º, 72, 83º). We collected five trials for each combination of θ_{wing} and θ_{leg}. This resulted in a resulted in a total of 60 trials.

We characterized how the wing and leg actuation angles changed over time during an attempt in a separate experiment. We attached BEETag markers (Crall et al., 2015) to the body frame and to each link actuated by the motors and tracked their positions using two calibrated high speed cameras (500 frame s^{-1}, 1080 × 1080 pixels) as the robot actuated its wings and legs during self-righting. We obtained 3-D kinematics of the markers using the Direct Linear Transformation method (Hedrick, 2008). We then measured the rotation of the link actuated by each motor about its axis as a function of time during an attempt. Because the wings were controlled to roll and pitch by the same angle, we used the average measured wing actuation profile (Figure 10B, dashed) of all the four motors. Note that the actual wing opening angle was smaller than the commanded (solid red) due to the inertia of robot body components attached to each motor.

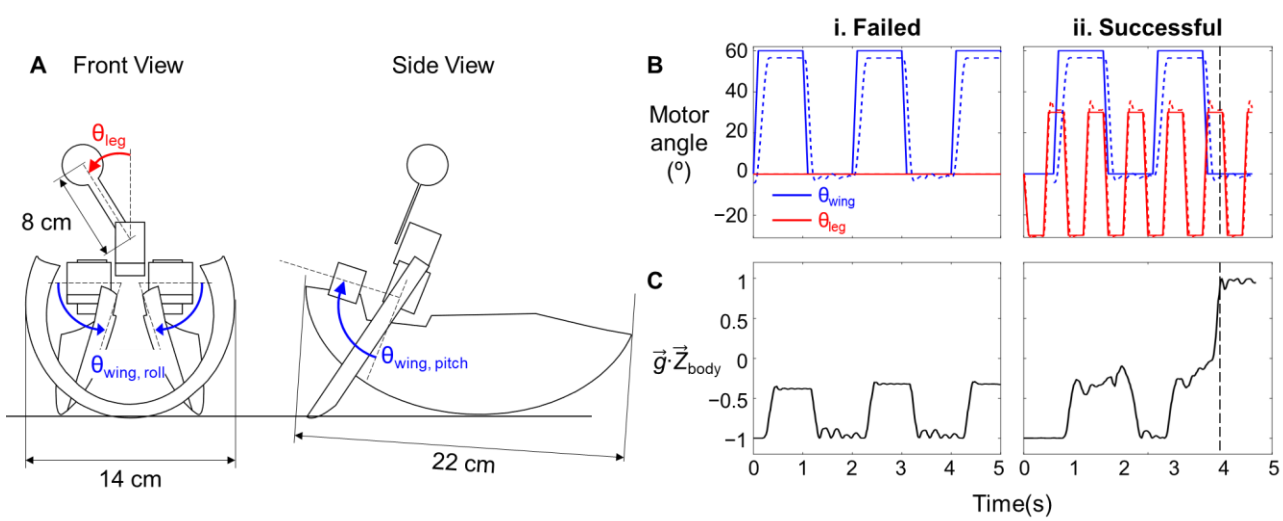

Figure 10. Robot design, actuation, and sensing. (**A**) Schematic of leg-assisted, winged self-righting robot from front and side views with geometric dimensions. Front view illustrates wing rolling and leg oscillation and side view illustrates wing pitching. (**B**) Motor actuation profile for wing (blue) and leg (red) as a function of time. Solid and dashed curves show commanded and measured motor actuation profiles, respectively. (**C**) Projection of gravitational acceleration $\vec{g}$ on body Z axis $\vec{Z}_{\text{body}}$ measured by onboard IMU as a function of time. Dashed line shows the instant when the body self-righted. In B, C, columns i and ii are for a representative failed and successful trial, respectively. Source: Figure_10BC_Source_Data.

Self-righting outcome and performance

For each animal trial, we watched the videos to determine whether the animal self-righted. Because the animal did not always immediately begin to self-right when placed on the arena (Camhi, 1977; Li et al., 2019), we defined the beginning of the self-righting attempt as the instant when the animal began moving its body or appendages to self-right. We defined the animal to have successfully self-righted if it attained an upright orientation with all six legs on the ground within 10 s of starting its attempt. We identified the successful trials that used the leg-assisted, winged strategy. For each animal and each leg treatment, we defined and measured its self-righting probability as the number of trials that self-righted using winged attempts divided by the total number of trials (five). We then found the self-righting probability for each leg treatment by averaging across all animals (Figure 2B).

For each robot trial, we measured the robot's 3-D orientation (Figure 10C) with respect to the lab frame (Figure 1D) using Euler angles (yaw α, pitch β, and roll γ, $Z{-}Y'{-}X''$ Tait-Bryan convention). We defined the beginning of the righting attempt as the instant when the robot started opening its wings and measured this from the time-stamped motor actuation commands (Figure 10Bii, Movie 5, top right). We defined the robot to have successfully self-righted if it attained an upright orientation within 10 s (five wing actuation cycles). We used the IMU to measure the projection of the gravity acceleration $\vec{g}$ onto the body Z axis $\vec{Z}_{\text{body}}$ as a function of time. This allowed us to determine when the robot became upright (Figure 1D).

We then counted the number of attempts required to self-right for all successful trials. Among all the 134 attempts observed across all 60 trials, 44 attempts succeeded, and 90 attempts failed.

Animal kinetic energy fluctuation

To measure kinetic energy fluctuation during self-righting attempts, in a separate experiment, we used three high speed cameras (Photron FASTCAM Mini UX-100) to record an animal's self-righting attempt at 2000 frames s^{-1}, first with its hind legs intact and then modified. For both hind legs, we used DeepLabCut (Mathis et al., 2018) to track their tip and femur-tibia joint. We also tracked the anterior tip of the head, the posterior tip of the abdomen and the midpoint of the body along the sagittal plane. We used the latter to approximate the middle of coxa-trochanter joints of both hind legs (Kram et al., 1997). We then used Direct Linear Transformation (Hedrick, 2008) to reconstruct 3-D motion of the tracked points.

To calculate kinetic energy fluctuation, we approximated each hind leg as two rigid rods connected by spherical joints. connected to the body by a spherical joint. Similarly, the tarsi and metatarsi of the hind leg were approximated a the One of the rods, which is connected to the body via a connected straight with variable length rotating about the coxa-trochanter joint (approximated as a spherical joint) (Figure 10B). For animals with leg modification, we approximated the stainless steel spheres at the leg tip as a point mass attached to the end of rod (Figure 10B). We defined kinetic energy fluctuation as the sum of kinetic energy from translational and rotational velocity components of both hind legs and the attached sphere (for modified legs) due to motion out of sagittal plane. For both hind legs, we measured the rotational velocities ω_x and ω_z about the body longitudinal (x) and vertical (z) axes, respectively, and translational velocity v_y of leg tips perpendicular to sagittal plane, all relative to the body frame attached to the middle of both coxa-trochanter joints. We then measured the kinetic energy fluctuation of a hind leg as:

$$KE_{\text{fluctuation}} = \frac{1}{2}\frac{m_{\text{rod}}}{3}(l_{yz}^2\omega_x^2 + l_{xy}^2\omega_z^2) + \frac{1}{2}m_{\text{sphere}}v_y^2 \quad (1)$$

where m_{rod} is the mass the rod, l_{yz} and l_{xy} are the projected lengths of the rod on *y-z* and *x-y* planes respectively, and m_{sphere} is the added spherical mass. We used the total mass of a hind leg (0.03 g (Kram et al., 1997)) for m_{rod}. m_{sphere} = 0.13 g for modified legs and zero for intact legs.

The kinetic energy fluctuation from leg flailing increased by six times (Figure 10C, D) when legs were modified. Although the added mass reduced the frequency of leg flailing (measured using oscillation of the vertical position of leg tip) by two times (Figure 10C), it was far outweighed by the effect of increased mass (12 times heavier than the intact leg). We averaged roll kinetic energy over the recorded interval (1s) to estimate kinetic energy fluctuation from leg flailing (Figure 2A).

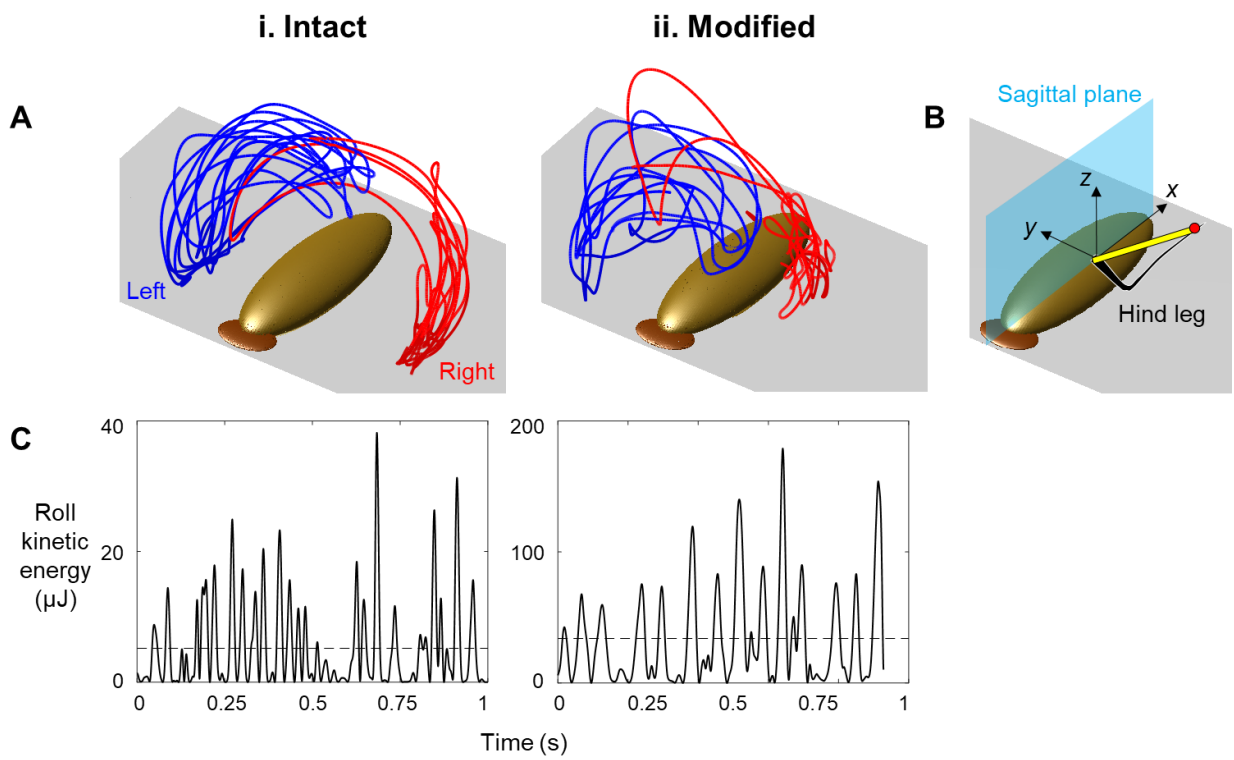

Figure 11. Animal kinetic energy fluctuation. (**A**) 3-D trajectory of flailing hind leg tips of animal with intact and modified hind legs. Blue and red curves are for left and right hind legs. (**B**) Approximating a hind leg (black) as a rigid rod (yellow) attached to body and the added mass at leg tip as a point mass (red). Body frame (*x-y-z*) and sagittal plane (blue) are shown. Body midline axis is along *x*-axis. (**C**) Roll kinetic energy

of flailing hind legs as a function of time for animal with intact and modified legs. Dashed lines show average roll kinetic energy. Source: Figure_11AC_Source_Data.

Robot 3-D motion reconstruction

For each robot trial, we reconstructed the robot's 3-D motion using the measured motor actuation profile (Figure 10 B, C) and 3-D orientation from IMU. We divided each trial into 0.01 s intervals and used the measured motor actuation angles and the measured Euler angles from IMU at that interval to reconstruct the robot shape and 3-D orientation, respectively. Because the IMU measured only the 3-D orientation of the robot (Figure 1D), we constrained the robot body to translate along the vertical direction (Figure 1D, *z* axis of lab frame) while maintaining contact with the ground (Movie 7). We then used the reconstructed 3-D motion of the robot to estimate the translational and rotational velocity components of all the robot parts.

Robot kinetic energy fluctuation

For each robot trial, we measured pitch and roll kinetic energies for all attempts. We defined pitch and roll kinetic energies as the kinetic energy of the entire robot due to their translational and rotational velocities within (v_x, v_z, and ω_y) and out of (ω_x, ω_z, and v_y) the sagittal plane.

Because the five motors, the leg rod, and the leg mass were all regularly shaped, we considered each as a solid object. Then, using their reconstructed 3-D motion, we calculated the pitch and roll kinetic energies for each of the seven solid objects as:

$$KE_{\text{pitch, object}} = \frac{1}{2}I_{yy}\omega_y^2 + \frac{1}{2}m(v_x^2 + v_z^2) \tag{2}$$

$$KE_{\text{roll, object}} = \frac{1}{2}(I_{xx}\omega_x^2 + I_{zz}\omega_z^2) + \frac{1}{2}mv_y^2 \tag{3}$$

where I_{xx}, I_{yy}, and I_{zz} are the principal moments of inertia of the solid object (measured at their center of mass), m is the mass of the solid object, and v_x, v_y, and v_z are the translational and ω_x, ω_y, and ω_z are the rotational velocity components of the solid object, respectively. All velocity components are measured

relative to the body frame. To calculate the moment of inertia, we approximated the motors and leg rod as solid cuboids and leg added mass as a solid sphere, all with uniform mass distribution.

For both the wings and head with complex shapes, we approximated them with uniformly distributed point mass clouds and calculated the pitch and roll kinetic energy for each point cloud as:

$$KE_{\text{pitch, cloud}} = \frac{1m}{2k} \sum_{i=1}^{k} (v_{x,i}^2 + v_{z,i}^2) \tag{4}$$

$$KE_{\text{roll, cloud}} = \frac{1m}{2k} \sum_{i=1}^{k} v_{y,i}^2 \tag{5}$$

where m is the total mass of the wing or head, k is the number of point masses in the point cloud, and $v_{x,i}$, $v_{y,i}$, and $v_{z,i}$ are the velocity components of the ith point mass.

To obtain the total pitch and roll kinetic energies of the robot, we added the pitch and roll kinetic energies of the five motors, the leg rod and mass, the two wings, and the head. To compare pitch and roll kinetic energy at each combination of θ_{wing} and θ_{leg}, we first averaged the pitch and roll kinetic energies during the phase when wings were fully held open in the first attempt of each trial and then averaged across the five trials at each combination (Figures 2A, 12).

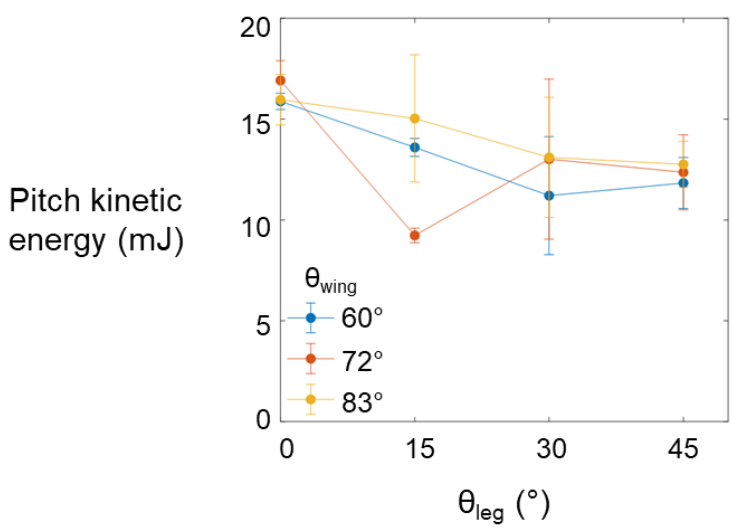

Figure 12. Pitch kinetic energy. Pitch kinetic energy of robot as a function of θ_{leg} at different θ_{wing}. Error bars are ± s.d. n = 20 trials at each θ_{wing}. Source: Figure_12_Source_Data.

Potential energy landscape model

The robot's gravitational potential energy is:

$$E = mgz_{CoM} \tag{6}$$

where m is the total mass of the robot, g is gravitational acceleration, z_{CoM} is center of mass height from the ground. To determine the center of mass, we used a CAD model of the robot (Figures 4A, 10A) and measured the 3-D positions of all robot body parts for a given body orientation and wing opening. Because the robot rarely lifted off during self-righting, in the model we constrained the lowest point of the robot to be always in contact with the ground.

The potential energy depended on body pitch and roll, wing opening angle, and leg oscillation angle. Because the effect of leg oscillation was modelled using kinetic energy fluctuation, we set the leg to be held fixed

in the middle when calculating the energy landscape[3]. Because we used Euler angles for 3-D rotations, change in body yaw did not affect z_{CoM}. We varied wing opening angle within the range [0º, 90°] with 0.5° increment. For each wing opening angle, we then varied both body pitch and roll within the range [−180°, 180°] with 1° increment and calculated z_{CoM} to obtain the system potential energy for each combination of body pitch and roll (Figure 4B).

[3] We verified that, whether the leg was held fixed or moving, there was only a very small change in the potential energy landscape.

System state trajectories on potential energy landscape

To visualize how the measured system state behaved on the landscape, we first discretized each righting attempt into time intervals of 0.01 s. For each interval, we used the measured the wing opening angle (Figure 10B, dashed blue curves) to calculate the potential energy landscape (Movie 5, top). We then projected the measured body pitch and roll onto the landscape over time to obtain the system state trajectory (Figure 5). Note that only the end point of the trajectory, which represents the current state, showed the actual potential energy of the system at the corresponding wing opening angle. The rest of the visualized trajectory showed how body pitch and roll evolved but, for visualization purpose, was simply projected on the landscape surface.

Potential energy barriers to self-right

We measured the potential energy barrier that must be overcome to escape from metastable local minimum to transition to an upright basin (Figure 4C, 6, Movie 6, bottom). For the measured wing opening angle (Figure 10B, dashed blue) and the corresponding potential energy landscape calculated at each time interval (see previous section), we considered imaginary straight paths away from the metastable local minimum (Figure 4B, white dot) in the full pitch-roll space, parameterized by an angle ψ relative to the positive pitch direction (body pitching up; Figure 4Ci). Along each imaginary straight path, we obtained a cross section of the landscape. Then, we measured and defined the maximal increase in potential energy in the cross section as the potential energy barrier along this imaginary straight path, which was a function of ψ, as shown by the polar plots in Figure 4C. We defined the roll barrier as the lowest escape barrier within $\psi = \pm [45°, 135°]$. We defined the pitch barrier as the escape barrier at $\psi = 0°$, i.e., towards the direction of the pitch minimum. We measured both roll and pitch barriers as a function of θ_{wing} (Figure 6).

Energy budget for self-righting transition

To understand how excess kinetic energy facilitates and determines self-righting transitions, we compared them to potential energy barriers. For transition to the pitch upright basin, we defined pitch mechanical energy budget as the difference between pitch kinetic energy and pitch barrier (Figure 7A-C). For transition to the roll upright basin, we defined roll mechanical energy budget as the difference between roll kinetic energy and the roll barrier (Figure 8A-C). For each attempt, we measured how pitch and roll mechanical energy budgets (Figures 7D, 8D) changed over time. Then we compared them between successful (Figures 7i, 8i) and failed (Figures 7ii, 8ii) attempts. For the duration of each wing opening attempt when the wings are held fully open, we measured the maximal mechanical energy budget. To compare how maximal mechanical energy budget varied with θ_{wing} and θ_{leg}, we then averaged it across all attempts at each combination of θ_{wing} and θ_{leg} (Figures 7E, 8E).

Statistics

We tested whether the animal's percentage of time spent on winged and legged self-righting attempts and probability depended on leg modification using a mixed-design ANOVA, with leg treatment as the fixed factor and individual as a random factor to account for individual variability.

We tested whether the robot's self-righting probability, number of attempts to self-right, pitch and roll kinetic energies, depended on θ_{leg}, at each θ_{wing}, using a chi-squared test for probability and an ANOVA for the rest, with θ_{leg} as a fixed factor. We tested whether pitch and roll mechanical energy budgets depended on θ_{wing} (at each θ_{leg}) and θ_{leg} (at each θ_{wing}) using ANOVAs with θ_{wing} and θ_{leg} as fixed factors, respectively. All data are reported as means ± 1 standard deviation (s.d.). All statistical tests were performed using JMP Pro 14 (SAS Institute Inc., NC, USA).

Acknowledgements

We thank Sean Gart, Thomas Mitchel, and Noah Cowan for discussion and Sean Gart for help with high-speed imaging and statistics. This work is funded by an Army Research Office Young Investigator Award, a Burroughs Wellcome Fund Career Award at the Scientific Interface, and The Johns Hopkins University Whiting School of Engineering start-up funds to C.L.

Additional information

Funding

Funders[4]	**Grant reference number**	**Author**
Army Research Office	W911NF-17-1-0346	Chen Li
Burroughs Wellcome Fund	1014584.01	Chen Li
Johns Hopkins University		Chen Li

[4] The funders had no role in the study design, data collection and interpretation, or the decision to submit the work for publication

Author contributions

R.O. designed study, developed robot, performed experiments, analyzed data, developed model, and wrote the paper; Q.X. developed preliminary model; C.L. designed and supervised study and revised the paper.

Competing interests

None declared.

Supplementary materials

Captions for Movies

Movie 1. Strenuous winged self-righting in discoid cockroach. A discoid cockroach makes multiple failed attempts to pitch over the head by opening and pushing its wings against the ground and eventually rolls to self-right.

Movie 2. Leg flailing during strenuous winged self-righting in discoid cockroach. A discoid cockroach opening and pushing its wings against ground and flailing its legs to self-right from a metastable state. Blue and red curves show trajectories of hind leg tips. Green arrows show contact points forming triangular base of support.

Movie 3. Robotic physical model. Wings can both pitch and roll relative to body. Leg oscillation emulates leg flailing of animal (inset).

Movie 4. Leg flailing kinetic energy fluctuation facilitates winged self-righting of animal. Representative trials of strenuous, leg-assisted, winged self-righting with and without hind leg modification (played three times).

Movie 5. Leg flailing kinetic energy fluctuation facilitates winged self-righting of robot. Left: Representative videos from top and front views. Top right: Commanded (solid) and measured (dashed) motor angles as a function of time. Blue and red curves are for wing and leg motors, respectively. Bottom right: Projection of gravitational acceleration $\vec{g}$ on body Z axis as a function of time, measured by onboard IMU. Video first shows a failed trial of without leg oscillation and then shows a successful trial with leg oscillation.

Movie 6. Potential energy landscape modeling. Top left: Illustrative robot body motion for self-righting via pitch and roll modes. Top right: Evolution of potential energy landscape as wings open, with robot state (dot) and trajectory. Black curve is for robot opening its wings and becoming trapped in metastable basin. Blue dashed and red solid curves are for robot escaping metastable basin via pitch and roll modes, respectively. Bottom right: Potential energy barrier to escape from upside-down or metastable local minimum along all directions in body pitch-roll space. Green arrow shows direction of pitch upright minima at pitch = 180°. Blue and red error bars show pitch kinetic energy and roll kinetic energy fluctuation. Bottom left: Pitch (blue) and roll (red) barrier as a function of wing opening amplitude θ_{wing}. Blue and red dashed lines show pitch kinetic energy and roll kinetic energy fluctuation, respectively. Gray band shows range of θ_{wing} tested.

Movie 7. Robot state trajectories on potential energy landscape. Top left: Representative trial. Bottom left: reconstructed 3-D motion. Right: Potential energy landscape with current robot state (dot) and state trajectory. Video first shows a failed trial without leg oscillation and then shows a successful trial with leg oscillation.

Movie 8. Robot state trajectory ensemble on potential energy landscape. Evolution of potential energy landscape and robot state trajectories during self-righting attempts. White and black curves show trajectories for successful and failed self-righting attempts, respectively. Green and pink dots show system state for successful and failed attempts, respectively. The high body roll of state trajectories as reaches maximal body pitch in failed attempts is an artifact from the singularity in Euler angle convention at near 90° body pitch.

Supplementary data files

Figure_2B_Source_Data: Animal self-righting probability. Data for all 30 individuals from 300 trials for both leg treatments (spreadsheet).

Figure_3_Source_Data: Robot self-righting performance. Robot's self-righting result, number of attempts, and roll kinetic energy for all 60 trials (spreadsheet).

Figure_4_Source_Data: Energy landscape modelling. Robot's potential energy landscape (Bi-iii) and potential energy barrier (Ci-iii) along all directions in the roll-pitch space (MATLAB figures).

Figure_5_Source_Data: Robot state trajectories on potential energy landscape. State trajectories for successful (i) and failed (ii) attempts at the three wing opening amplitudes tested (MATLAB figures).

Figure_6_Source_Data: Robot transition barriers for self-righting. Potential energy of the robot (as a function of (A) body pitch and wing opening angle and (B) body roll and wing opening angle) and roll and pitch barriers for the robot (C). (MATLAB figures (A, B), spreadsheet (C)).

Figure_7_Source_Data: Pitch mechanical energy budget. Data for all 134 attempts (spreadsheet).

Figure_8_Source_Data: Roll mechanical energy budget. Data for all 134 attempts (spreadsheet).

Figure_9_Source_Data: Animal's percentage of time spent on legged and winged attempts. Data for all 30 individuals from 300 trials for both leg treatments (spreadsheet).

Figure_10BC_Source_Data: Representative wing opening and leg oscillation angles and orientation data recorded for robot. Data given for representative failed and successful attempts (spreadsheet).

Figure_11AC_Source_Data: Animal's hind leg 3-D trajectories and roll kinetic energy as a function of time. Data for intact and modified animal are given (spreadsheet).

Figure_12_Source_Data: Robot pitch kinetic energy. Data given for all 60 trials (spreadsheet).

References

Aguilar J, Zhang T, Qian F, Kingsbury M, McInroe B, Mazouchova N, Li C, Maladen R, Gong C, Travers M, Hatton RL, Choset H, Umbanhowar PB, Goldman DI. 2016. A review on locomotion robophysics: The study of movement at the intersection of robotics, soft matter and dynamical systems. *Reports Prog Phys* **79**:110001. doi:10.1088/0034-4885/79/11/110001

Ashe VM. 1970. The righting reflex in turtles : A description and comparison. *Psychon Sci* **20**:150–152.

Bartholomew GA, Caswell HH. 1951. Locomotion in Kangaroo rats and its adaptive significance. *J Mammal* **32**:155–169.

Berman GJ. 2018. Measuring behavior across scales. *BMC Biol* **16**:23. doi:10.1186/s12915-018-0494-7

Bolmin O, Duan C, Urrutia L, Abdulla AM, Hazel AM, Alleyne M, Dunn AC, Wissa A. 2017. Pop! Observing and Modeling the Legless Self-righting Jumping Mechanism of Click Beetles. Springer, Cham. pp. 35–47. doi:10.1007/978-3-319-63537-8_4

Brackenbury J. 1990. A novel method of self-righting in the springtail Sminthurus viridis (Insecta: Collembola). *J Zool* **222**:117–119. doi:10.1111/j.1469-7998.1990.tb04033.x

Bryngelson JD, Wolynes PG. 1989. Intermediates and barrier crossing in a random energy model (with applications to protein folding). *J Phys Chem* **93**:6902–6915. doi:10.1021/j100356a007

Camhi JM. 1977. Behavioral switching in cockroaches: transformations of tactile reflexes during righting behavior. *J Comp Physiol* **113**:283–301. doi:10.1007/BF00620403

Caporale JD, Mcinroe BW, Ning C, Libby T, Full RJ, Koditschek DE. 2019. Coronal Plane Spine Twisting Composes Shape To Adjust the Energy Landscape for Grounded ReorientationIcra. pp. 9–16.

Crall JD, Gravish N, Mountcastle AM, Combes SA. 2015. BEEtag: A low-cost, image-based tracking system for the study of animal behavior and locomotion. *PLoS One* **10**:1–13. doi:10.1371/journal.pone.0136487

Creery BL, Bland BH. 1980. Ontogeny of fascia dentata electrical activity and motor behavior in the dutch belted rabbit (Oryctolagus cuniculus). *Exp Neurol* **67**:554–572. doi:10.1016/0014-4886(80)90126-0

Davis WJ. 1968. Lobster righting responses and their neural control. *Proc R Soc B* **170**:435–456. doi:10.1098/rspb.1968.0049

Delcomyn F. 1987. Motor activity during searching and walking movements of cockroach legs. *J Exp Biol* **133**:111–120.

Dickinson MH, Farley CT, Full RJ, Koehl MAR, Kram R, Lehman S. 2000. How animals move: An integrative view. *Science* **288**:100–106. doi:10.1126/science.288.5463.100

Domokos G, Várkonyi PL. 2008. Geometry and self-righting of turtles. *Proc Biol Sci* **275**:11–17. doi:10.1098/rspb.2007.1188

Frantsevich LI, Mokrushov PA. 1980. Turning and righting inGeotrupes (Coleoptera, Scarabaeidae). *J Comp Physiol* **136**:279–289. doi:10.1007/BF00657348

Full RJ, Tu MS. 1990. Mechanics of six-legged runners. *J Exp Biol* **148**:129–146.

Full RJ, Yamauchi A, Jindrich DL. 1995. Maximum single leg force production: Cockroaches righting on photoelastic gelatin. *J Exp Biol* **198**:2441–2452.

Golubović A, Tomović L, Ivanović A. 2015. Geometry of self righting: The case of Hermann's tortoises. *Zool Anz* **254**:99–105. doi:10.1016/j.jcz.2014.12.003

Gould S, Vrba E. 1982. Exaptation—a missing term on the science of form. *Paleobiology*. doi:10.1017/S0094837300004310

Hailey A, Theophilidis G. 1987. Cardiac responses to stress and activity in the armoured legless lizard Ophisaurus apodus: Comparison with snake and tortoise. *Comp Biochem Physiol -- Part A Physiol* **88**:201–206. doi:10.1016/0300-9629(87)90470-1

Hanggi P. 1986. Escape from a metastable state. *J Stat Phys* **42**:105–148. doi:10.1007/BF01010843

Hedrick TL. 2008. Software techniques for two- and three-dimensional kinematic measurements of biological and biomimetic systems. *Bioinspir Biomim* **3**:034001. doi:10.1088/1748-3182/3/3/034001

Hoffman D. 1980. Defensive Responses of Marine Gastropods (Prosobranchia, Trochidae) to Certain Predatory Seastars and the Dire Whelk, Searlesia dira (Reeve) **34**.

Johnson AM, Libby T, Chang-Siu E, Tomizuka M, Full RJ, Koditschek DE. 2012. Tail assited dynamic self rightingAdaptive Mobile Robotics. World Scientific. pp. 611–620. doi:10.1142/9789814415958_0079

Kessens CC, Smith DC, Osteen PR. 2012. A framework for autonomous self-righting of a generic robot on sloped planar surfaces. *Proc - IEEE Int Conf Robot Autom* 4724–4729. doi:10.1109/ICRA.2012.6224770

Kleitman N, Koppányi T. 1926. Body-righting in the fowl (Gallus domesticus). *Am J Physiol* **78**:111–123.

Koppányi T, Kleitman N. 1927. Body righting and related phenomena in the domestic duck (Anas boscas). *Am J Physiol Content* **82**:672–685. doi:10.1152/ajplegacy.1927.82.3.672

Kovac M, Fuchs M, Guignard A, Zufferey J-C, Floreano D. 2008. A miniature 7g jumping robot2008 IEEE International Conference on Robotics and Automation. IEEE. pp. 373–378. doi:10.1109/ROBOT.2008.4543236

Kram R, Wong B, Full RJ. 1997. Three-dimensional kinematics and limb kinetic energy of running cockroaches. *J Exp Biol* **200**:1919–1929.

Kramers HA. 1940. Brownian motion in a field of force and the diffusion model of chemical reactions. *Physica* **7**:284–304. doi:10.1016/S0031-8914(40)90098-2

Li C, Kessens CC, Fearing RS, Full RJ. 2017. Mechanical principles of dynamic terrestrial self-righting using wings. *Adv Robot*. doi:10.1080/01691864.2017.1372213

Li C, Kessens CC, Young A, Fearing RS, Full RJ. 2016. Cockroach-inspired winged robot reveals principles of ground-based dynamic self-rightingIEEE International Conference on Intelligent Robots and Systems. pp. 2128–2134. doi:10.1109/IROS.2016.7759334

Li C, Pullin AO, Haldane DW, Lam HK, Fearing RS, Full RJ. 2015. Terradynamically streamlined shapes in animals and robots enhance traversability through densely cluttered terrain. *Bioinspir Biomim* **10**:46003. doi:10.1088/1748-3190/10/4/046003

Li C, Wöhrl T, Lam HK, Full RJ. 2019. Cockroaches use diverse strategies to self-right on the ground. *J Exp Biol* **222**:jeb186080. doi:10.1242/jeb.186080

Malashichev Y. 2016. Asymmetry of righting reflexes in sea turtles and its behavioral correlates. *Physiol Behav* **157**:1–8. doi:10.1016/j.physbeh.2016.01.001

Mathis A, Mamidanna P, Cury KM, Abe T, Murthy VN, Mathis MW, Bethge M. 2018. DeepLabCut: markerless pose estimation of user-defined body parts with deep learning. *Nat Neurosci* **21**:1281–

1289. doi:10.1038/s41593-018-0209-y

Othayoth R, Thoms G, Li C. 2020. An energy landscape approach to locomotor transitions in complex 3D terrain. *Proc Natl Acad Sci* **117**:14987–14995. doi:10.1073/pnas.1918297117

Penn D, Brockmann HJ. 1995. Age-biased stranding and righting in male horseshoe crabs, Limulus polyphemus. *Anim Behav* **49**:1531–1539. doi:10.1016/0003-3472(95)90074-8

Quigley M, Conley K, Gerkey B, Faust J, Foote T, Leibs J, Berger E, Wheeler R, Mg A. 2009. ROS: an open-source Robot Operating System. *Icra* **3**:5. doi:http://www.willowgarage.com/papers/ros-open-source-robot-operating-system

Ribak G, Weihs D. 2011. Jumping without using legs: The jump of the click-beetles (Elateridae) is morphologically constrained. *PLoS One* **6**:1–7. doi:10.1371/journal.pone.0020871

Robins A, Lippolis G, Bisazza A, Vallortigara G, Rogers LJ. 1998. Lateralized agonistic responses and hindlimb use in toads.

Sherman E, Novotny M, Camhi JM. 1977. A modified walking rhythm employed during righting behavior in the cockroach Gromphadorhina portentosa. *J Comp Physiol A* **113**:303–316. doi:10.1007/BF00620404

Silvey GE. 1973. Motor Control of Tail Spine Rotation of the Horseshoe Crab, Limulus Polyphemus. *J Exp Biol* **58**:599–625.

Springthorpe D. 2016. Biomechanical Multifunctionality in the Ghost Crab, Ocypode quadrata. University of California, Berkeley.

Steyermark AC, Spotila JR. 2001. Body Temperature and Maternal Identity Affect Snapping Turtle (Chelydra serpentina) Righting Response. *Copeia* **2001**:1050–1057. doi:10.1643/0045-8511(2001)001[1050:btamia]2.0.co;2

Vince MA. 1986. Response of the newly born clun forest lamb to maternal vocalizations. *Behaviour* **96**:164–170.

Weldon PJ, Hoffman DL. 1979. Kick and Thrust Foot Movements in the Righting and Escape Behavior of Marine Prosobranch Gastropods (Mollusca: Gastropoda). *Z Tierpsychol* **50**:387–398. doi:10.1111/j.1439-0310.1979.tb01039.x

Winters WD, Hance AJ, Cadd GC, Lakin ML. 1986. Seasonal and sex influences on ketamine-induced analgesia and catalepsy in the rat; a possible role for melatonin. *Neuropharmacology* **25**:1095–1101. doi:10.1016/0028-3908(86)90156-5

Xuan Q, Li C. 2020. Randomness in appendage coordination facilitates strenuous ground self-righting. *Bioinspir Biomim* **21**:1–9. doi:10.1088/1748-3190/abac47

Zill SN. 1986. A model of pattern generation of cockroach walking reconsidered. *J Neurobiol* **17**:317–328. doi:10.1002/neu.480170406